Scale-resolving simulations of the flow in the Francis-99 turbine at part-load condition

Scale-resolving simulations of the flow in the Francis-99 turbine at part-load condition

IOP Conf. Series: Earth and Environmental Science 1079 (2022) 012085 doi:10.1088/1755-1315/1079/1/012085

Scale-resolving simulations of the flow in the Francis-99 turbine at part-load condition

Mohammad Hossein Arabnejad, Håkan Nilsson and Rickard E. Bensow

Department of Mechanics and Maritime Sciences, Chalmers University of Technology, 41296 Gothenburg, Sweden

E-mail: mohammad.h.arabnejad@chalmers.se

Abstract. In this paper, we investigate the formation of the Rotating Vortex Rope (RVR) using scale-resolving methods, SAS and Wall-Modeled LES (WMLES). We compare the results from these simulation methods with the experimental data of the Francis-99 workshop. This comparison shows that the general features of the RVR can be captured with both methods. However, using WMLES methods would lead to a better quantitative agreement between the velocity profiles in the draft tube in the simulation and the experiment. The reasons for this better agreement are discussed in detail. A comparison of the pressure fluctuations in the draft tube captured in the simulations and the experiment is also presented. This comparison shows that all simulations under-predict the Root Mean Square (RMS) of these pressure fluctuations, although the RMS values predicted by the WMLES simulation are closer to the experimental values.

1 Introduction

To be able to regulate renewable electric energy systems with a large share of intermittent energy sources and to meet the flexible electricity demand, hydraulic turbines are being operated at off-design conditions more often nowadays. In this type of operation, the flow in the different components of the hydraulic turbines is prone to complex flow behavior and instabilities. Specifically at part-load condition, a flow instability called Rotating Vortex Rope (RVR) is formed in the draft tube due to the residual swirl in the flow exiting the runner. This instability can produce significant pressure fluctuations leading to significant swing in the output of the hydro power plant [1, 2].

Due to the detrimental effects of the RVR for the safe off-design operation of hydro turbines, several numerical studies have been devoted to investigating the RVR in hydro turbines. A majority of these simulations were performed using Reynolds-averaged Navier–Stokes (RANS) approaches because of their low computational cost compared to scale-resolving methods. However, previous studies have shown that using RANS would lead to a fast decay of the swirling flow around the RVR and under-prediction of the pressure fluctuations caused by the RVR [3]. In the present paper, we investigate

the performance pf SAS and Wall-modeled LES (WMLES) to simulate the formation of RVRs in the Francis-99 turbine at a part-load condition. The numerical results are compared with the experimental data provided through the Francis-99 workshop, and the cause of the differences between the numerical results are explained in detail.

2 Numerical set-up

The governing equations are the incompressible Navier-Stokes equations for single-phase flows. Using either RANS or LES approach, the governing equations read

$$\nabla \cdot (\bar{\mathbf{u}}) = 0, \tag{1}$$

$$\frac{\partial}{\partial t}(\bar{\mathbf{u}}) + \nabla \cdot (\bar{\mathbf{u}} \otimes \bar{\mathbf{u}}) + \nabla \cdot (\frac{p}{\rho}\mathbf{I} - \nu S) + \nabla \cdot (-2\nu_{unres.}S + \frac{2}{3\rho}k_{unres.}\mathbf{I}) = 0, \tag{2}$$

where $\mathbf{u}$ is the velocity vector, p is the pressure, ρ is the density, $\mathbf{I}$ is the identity tensor, S is the strain tensor, and ν is the kinematic viscosity. In Eqs. 1 and 2, the bar operation on the velocity vector, $\bar{\mathbf{u}}$, represents a time-averaging operation or spatial filtering depending on whether a RANS or LES approach is used. As the result of this filtering or averaging, turbulent viscosity, $\nu_{unres.}$, and kinetic energy, $k_{unres.}$, due to unresolved turbulence appear in Eq. 2 which should be modelled. In this paper, we use the following two models to approximate these terms.

SST − SAS *RANS approach* Within the RANS context, $\nu_{unres.}$ and $k_{unres.}$ represent the turbulent viscosity, ν_t, and the turbulent kinetic energy, k_t, respectively. They are here assumed to be modelled using the Shear Stress Transport based Scale-Adaptive Simulation model (SST-SAS) [4, 5]. In this turbulence model, transport equations are used to obtain the turbulent kinetic energy, k_t, and the turbulent specific rate of dissipation, ω_t, which are then used to calculate ν_t as,

$$\nu_t = a_1 \frac{k_t}{\max(a_1\omega_t, b_1 F_{23} S)}, \tag{3}$$

where $\mathbf{S}$ is the invariant measure of the strain rate, a_1 and b_1 are constants, and F_{23} is a blending function. The transport equation for k_t is the same as the equation in the $\mathrm{k}-\omega$ SST turbulence model [6] while the transport equation for ω_t has an extra source term, Q_{SAS}, which can be read as

$$Q_{SAS} = \max\left[\rho\zeta_2\kappa S^2\left(\frac{L}{L_{vk}}\right)^2 - C\frac{2\rho k_t}{\sigma_\Phi} max\left(\frac{|\nabla\omega_t|^2}{\omega_t^2}, \frac{|\nabla k_t|^2}{k_t^2}\right), 0\right], \tag{4}$$

where ζ_2, κ, σ_Φ, and C are constants. In Eq. 4, L and L_{vK} are the modelled turbulence length scale and the von Karman length scale, respectively, which are defined as

$$L = \frac{\sqrt{k}}{c_\mu^{1/4}\omega}\,,\; L_{vK} = max\left(\frac{\kappa S}{|\nabla^2\tilde{\mathbf{u}}|}, C_s\sqrt{\frac{\kappa\zeta_2}{\beta/c_\mu - \alpha}}\right), \tag{5}$$

where c_μ, β, C_s and α are constants.

WALE WMLES approach In the WMLES approach, $\nu_{unres.}$ and $k_{unres.}$ are the sub-grid scale viscosity, ν_{sgs}, and the sub-grid turbulent kinetic energy, k_{sgs}, respectively. In the present work, we use the wall-adapting local eddy-viscosity (WALE) LES model proposed by Nicoud and Ducros [7], where these terms are modeled as

$$\nu_{sgs} = C_k \Delta \frac{\sqrt{k_{sgs}}}{\rho}, \tag{6}$$

$$k_{sgs} = \left(\frac{C_w^2 \Delta}{C_k}\right)^2 \frac{(\tilde{S}^d \tilde{S}^d)^3}{\left(\left(\tilde{S}\tilde{S}\right)^{5/2} + \left(\tilde{S}^d \tilde{S}^d\right)^{5/4}\right)^2}. \tag{7}$$

In Eqs. 6 and 7, Δ is the cell length scale and $C_k = 1.6$ and $C_w = 0.325$ are the model constants. $\tilde{S}$ and $\tilde{S}^d$ are also, respectively, the resolved-scale strain rate tensor and traceless symmetric part of the square of the velocity gradient tensor.

2.1 Discretization schemes and solution algorithm

The simulations in this paper are performed using a modified interPhaseChangeFoam solver [8, 9] from the OpenFOAM-2.2.x framework [10]. The convective terms in the momentum equations are discretized using the Linear-Upwind Stabilised Transport (LUST) convection scheme [11]. The diffusion terms in the momentum equations are discretized using the linear scheme. The discretized equations are solved using a pressure-based PIMPLE approach. To achieve convergence before phase averaging presented in this paper, the simulations are ran for the flow time corresponding to 30 revolutions of the runner. The time step in these simulations is set to 10^{-4}s.

3 The Francis-99 turbine and computational mesh

The so-called Francis-99 turbine [12] is used in the present study. The studied flow condition corresponds to the part-load (PL) condition in the second Francis-99 workshop. The guide vane opening in this condition is $\alpha = 6.72^o$, the runner angular speed is $n = 332.84$r/min, and the discharge is $Q = 0.13962\,\mathrm{m}^3/\mathrm{s}$, which corresponds to 69.9 % of the discharge at the best efficiency point (BEP). The computational domain for this turbine shown in Fig. 1 includes the spiral casing, the stay vanes, the guide vanes, the runner, and the draft tube. Table 1 shows the specifications of the meshes for the different components of the turbine. These meshes are created using the Pointwise V18.3 mesh generation software. As it can be seen in the table, the average y^+ value for all components is larger than 1, so the wall function based on Spalding's law [13] is used at the walls.

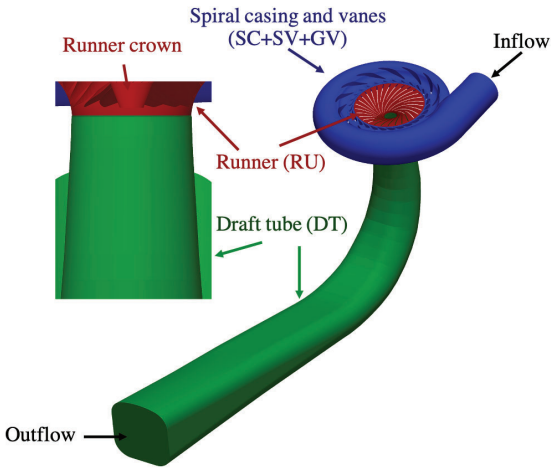

Figure 1: Computational domain.

Table 1: Mesh resolution.

Components	# of cells	Average y^+
SC+SV+GV	10.12 M	20
RU	5.13 M	12
DT	5.63 M	14
Total	20.88 M	17

As mentioned earlier, the experimental data from the second Francis-99 workshop is used for validation in the present study. This data includes both pressure and velocity measurements at the locations shown in Fig. 2a. The velocity measurements were done for the axial and horizontal components over three lines, Line 1, Line 2, and Line 3 in Fig. 2a. The pressure measurements were done at two probes in the draft tube, marked by Probe 2 and Probe 3 in Fig. 2a, and a probe in the vaneless region between the guide vane blades and runner blades, marked by Probe 1 in Fig. 2b.

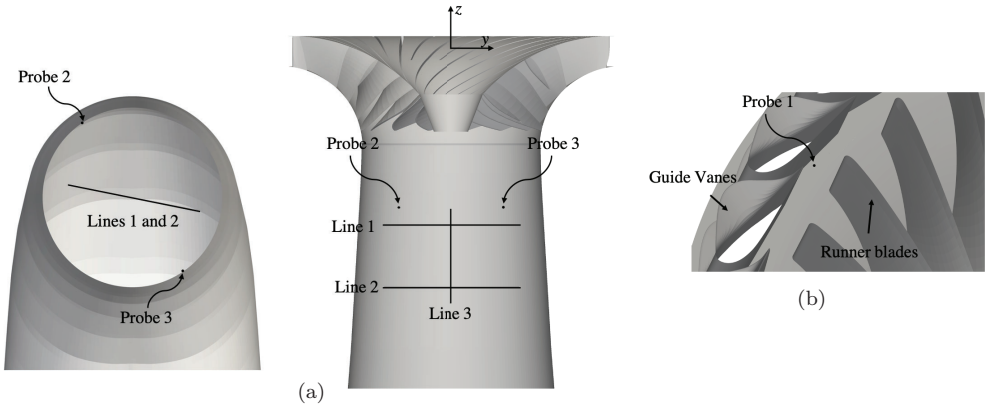

Figure 2: Locations of measurement probes and lines for the experimental data provided at the second Francis-99 workshop, a) Measurement probes and lines in the draft tube, b) probe between guide vanes and runner.

4 Results

The comparison between time-averaged velocities over the three lines shown in Fig. 2a is presented in Fig. 3. The profiles of axial velocity over Line 1 and Line 2 (Fig. 3a) show that there is a region of velocity deficit near the center of the draft tube ($-100\,\text{mm} < y < 100\,\text{mm}$) in the numerical and experimental results. It can be

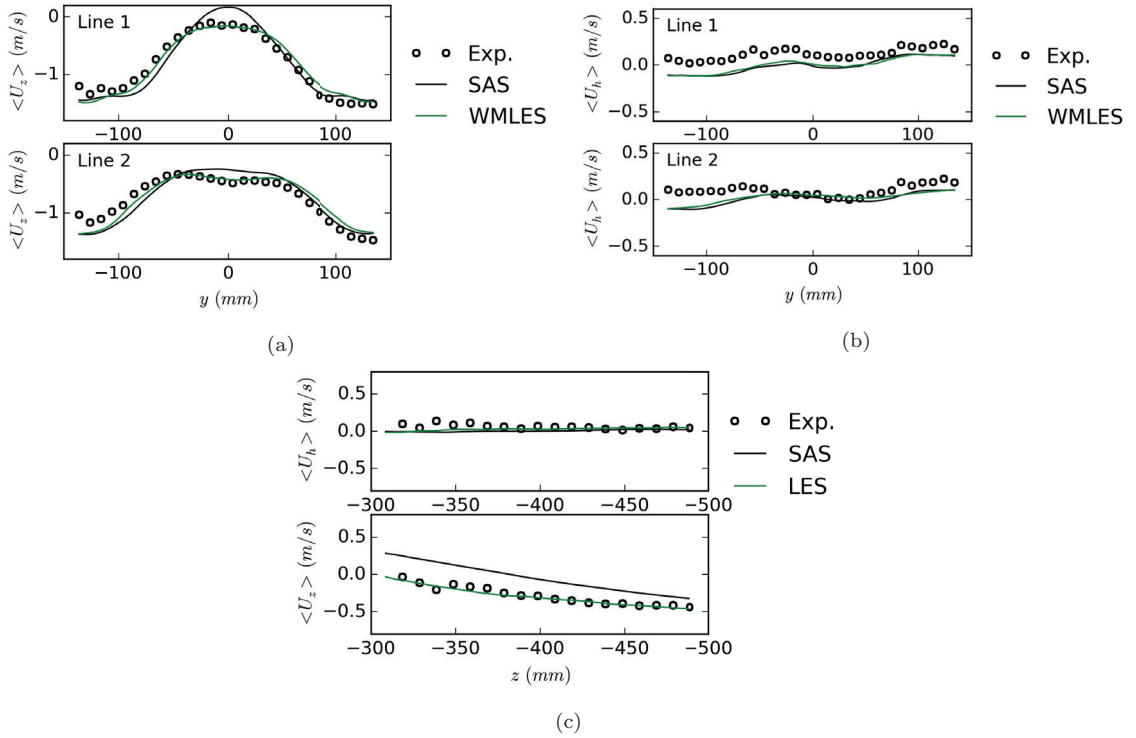

Figure 3: Comparison between the averaged velocities along the measurement lines in Fig. 2a in the experiment and the simulations, a) Axial velocity, Lines 1 (upper) and 2 (lower), b) Horizontal velocity, Lines 1 (upper) an 2 (lower), c) Axial (lower) and horizontal (upper) velocities, Line 3.

also seen that the choice turbulence modeling has an effect on radial extension of this region and its absolute axial velocities. In the WMLES results, the radial extension of this region is in better agreement with the experimental data as compared to the SAS results. Furthermore, while the WMLES simulation predicts negative values at the center of draft tube ($y = 0$) similar to the experiment, the SAS simulation predicts positive values in this region. This difference is more clear on the Line 3 in Fig. 3c where the averaged axial velocity over the centerline of the draft tube is presented. The reason for this difference will be explained later. The comparison of the the horizontal velocity profiles in Figs. 3b and 3c also show that the effect of choosing different turbulence modelings are smaller compared to the axial velocity profiles as both SAS and WMLES simulations predict similar velocity profiles.

To further compare the velocity profiles in the experiment and simulations, Fig. 4 presents the phase-averaged axial velocity over Lines 1 and 2 in the experimental and numerical results. In these figures, two instances are marked by A and B. The instance A is when the RVR is on the measurement lines and the instance B is when the RVR has left these lines. The comparison of the numerical and experimental results shows that both SAS and WMLES predict similar velocity profile compared the experiment at the instance A. At this instance, the axial velocity in the simulations and experiment is positive at the location of the RVR. At the instance B, however, the axial velocity is

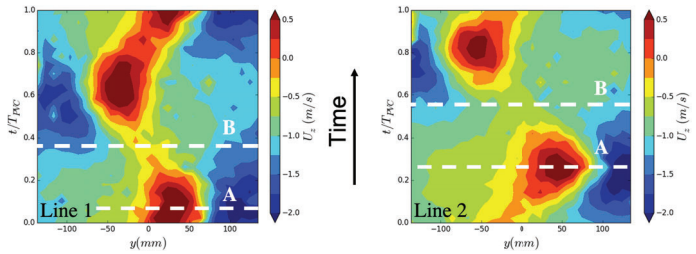

(a) Exp.

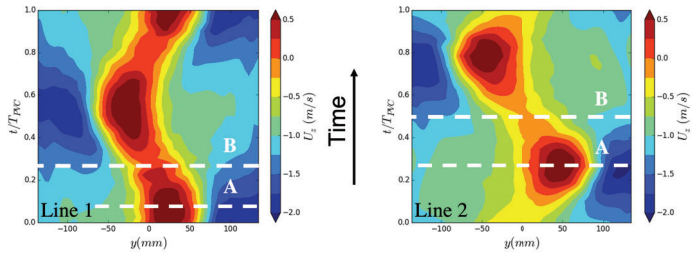

(b) SAS

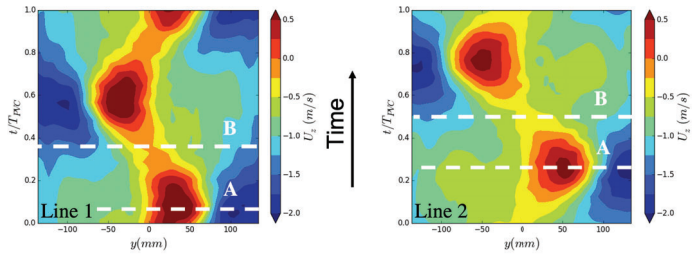

(c) WMLES

Figure 4: Phase-averaged values of axial velocity over Lines 1 and 2 in the experiment and simulations.

decreased since the RVR has rotated away from the measurement line. The comparison of the simulations for this instance shows that they predict different axial velocities. In the SAS simulation, the axial velocity at this instance is positive while the axial velocity in the WMLES is negative and similar to the experiment. The reason for this difference is that the RVR in the SAS simulation rotates close to the center of the draft tube. This means that even at instance B when the RVR rotates away from the measurement line, there are some parts of RVR that overlap with the measurement lines which leads to positive values of axial velocity. In the WMLES simulation and the experiment, however, the RVR leaves the measurement line completely at this instance meaning that there is almost no overlap between the measurement lines and the RVR. This in turn leads to the decrease in the axial velocity towards the negative values.

To compare the pressure fluctuations in the draft tube captured in the simulations and experiment, Fig. 5 presents these pressure fluctuations at Probe 2 shown in Fig. 2. This figure also includes the Root Mean Square (RMS) of the fluctuations for the simulations and experiment. The pressure fluctuation signal in the experiment shows the sinusoidal behavior which is due to the rotation of RVR. Similar behavior can be seen in the SAS and WMLES simulations. It can be, however, seen that both simulations

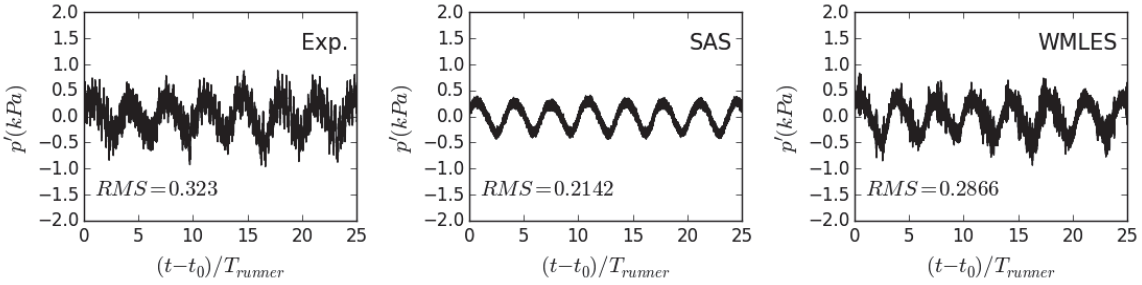

Figure 5: The signal of pressure fluctuations at Probe 2 shown in Fig. 2a in the experiment and simulations.

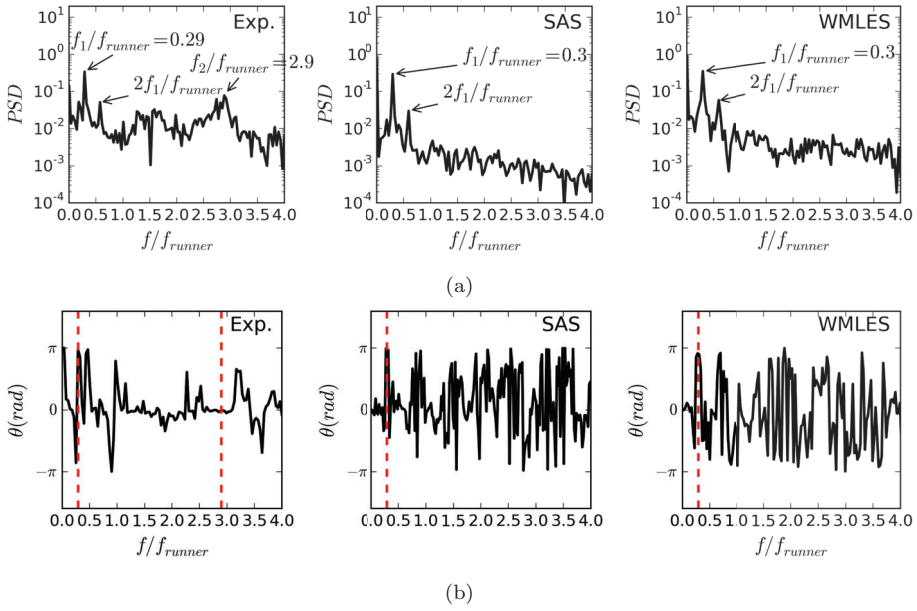

Figure 6: Spectral analysis of pressure signals from probes in the draft tube in the experiment and simulations, a) Frequency analysis of pressure signal from Probe 2, b) the phase difference between the pressure signals from Probes 2 and 3.

predict lower RMS values than the experimental one.

To further analyze the pressure fluctuations in the draft tube, Fig. 6a shows the frequency analysis of these pressure fluctuations. The phase difference between the pressure fluctuations signals from Probes 2 and 3 in the draft tube is also shown in 6b. The frequency analysis of the pressure fluctuations in the experiment indicates that there exists two dominant frequencies, f_1 and f_2. The phase difference for the frequency f_1 and its harmonic, $2f_1$ is π. This phase difference, and the fact that Probes 2 and 3 are located at opposite sides of the draft tube cone, suggests that this dominant frequency is due to the precession of the RVR in the draft tube cone. For the dominant frequency f_2, the phase difference is almost zero indicating that the corresponding pressure fluctuations are synchronous. The frequency analyses of the pressure signals in the simulations show that the dominant frequency of the RVR, f_1, and its harmonic, $2f_1$, is captured by both

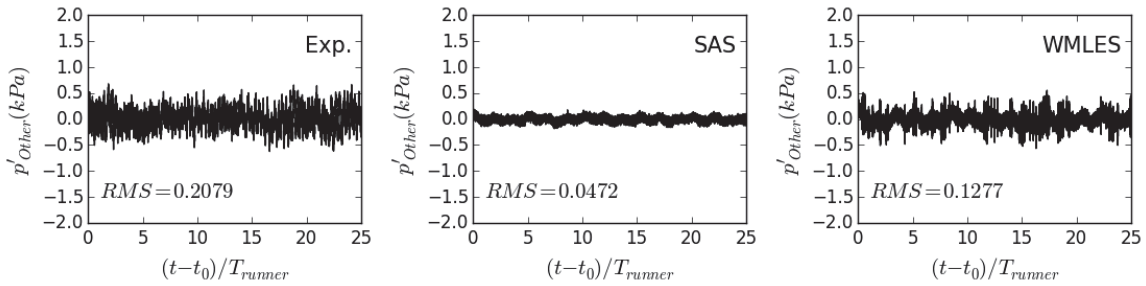

Figure 7: The signal of pressure fluctuations at Probe 2 without the effect of RVR in the experiment and simulations.

Simulations. The numerical results, however, lack the experimental dominant frequency f_2, which causes a reduced RMS value shown in Fig. 5.

Figure 7 shows the pressure signal without the effect of the RVR in the simulations and the experiment. To obtain this signal, the pressure signal are decomposed into the pressure signal due to the RVR and the pressure signal due to other sources. Similar decomposition can be seen in Arpe et al. [14], Favrel et al. [15]. It can be seen that the RMS value of the signal in the experiment is higher than the RMS values in both simulations. As mentioned before, the reason for this difference is that the signal in the experiment includes the fluctuations corresponding to the dominant frequency f_2. This type of fluctuations, however, is not present in the simulations which leads to under-prediction of the fluctuations in the simulations.

5 Conclusions

In this paper, we simulate the flow in the Francis-99 turbine at a part-load condition using two scale-resolving methods, SAS and Wall-modeled LES (WMLES). The main focus is to test how these methods can capture the velocity field and the pressure fluctuations in the draft tube in comparison with the experimental data provided by the Francis-99 workshop. The results show that both methods can capture the general features of the velocity field in the experiment, although the WMLES method provides a better quantitative agreement with the experimental data. The reason for this better agreement is revealed to be a better agreement between path of the vortex in the WMLES simulation and the one in the experiment. The comparison between the pressure fluctuations in the simulations and experiment shows that both methods predict a lower Root Mean Square (RMS) of the pressure fluctuations in the draft tube compared to the experiment. The reason for this under-prediction is investigated using the spectral analysis of the pressure fluctuations in the draft tube. This analysis reveals that the main reason is the synchronous pressure fluctuations at around 2.8 times the frequency of the runner which can be seen only in the experiment.

Acknowledgments

The work was funded by Chalmers Energy Area of Advance and was carried out as a part of the “Swedish Hydropower Centre - SVC”. SVC is established by the Swedish

Energy Agency, EnergiForsk and Svenska Kraftnät together with Luleå University of Technology, The Royal Institute of Technology, Chalmers University of Technology and Uppsala University, www.svc.nu. The computations were enabled by resources provided by the Swedish National Infrastructure for Computing (SNIC) at NSC and C3SE partially funded by the Swedish Research Council through grant agreement no. 2018e05973. The investigated test case is provided by NTNU, Norwegian University of Science and Technology, under the Francis-99 workshop series.

References

[1] W. Rheingans. *Transactions of the ASME*, 62:171–184, 1940.

[2] D. Valentín, A. Presas, E. Egusquiza, C. Valero, M. Egusquiza, and M. Bossio. *Energies*, 10(12):2124, 2017.

[3] A. Ruprecht, T. Helmrich, T. Aschenbrenner, and T. Scherer. In *IAHR Symposium on Hydraulic Machinery and Systems*, volume 1, pages 259–266. Lausanne, Switzerland, 2002.

[4] F. Menter and Y. Egorov. In *43rd AIAA aerospace sciences meeting and exhibit*, 2005.

[5] Y. Egorov and F. Menter. pages 261–270. Springer, 2008.

[6] F. Menter. In *23rd fluid dynamics, plasmadynamics, and lasers conference*, 1993.

[7] F. Nicoud and F. Ducros. *Flow Turbul. Combust.*, 62(3):183–200, 1999.

[8] R.E. Bensow and G. Bark. *J. Fluids Eng.*, 132(4):041302, 2010.

[9] A Asnaghi, A Feymark, and RE Bensow. *Int. J. Multiph. Flow*, 93:142–157, 2017.

[10] H. Weller, G. Tabor, H. Jasak, and C. Fureby. *Comput. Phys.*, 12(6):620–631, 1998.

[11] H. Weller. *Monthly Weather Review*, 140(10):3220–3234, 2012.

[12] C. Trivedi, M.J. Cervantes, B.K. Gandhi, and O.G. Dahlhaug. *J. Fluids Eng.*, 135 (11), 2013.

[13] D. Spalding. *Journal of Applied Mechanics*, 28(3):455–458, 1961.

[14] J. Arpe, C. Nicolet, and F. Avellan. *Journal of Fluids Engineering*, 131(8), 2009.

[15] A. Favrel, A. Müller, C. Landry, K. Yamamoto, and F. Avellan. *Experiments in Fluids*, 57(11):1–16, 2016.